

# Surface reconstruction of CoAl hydroxide electrodes for accelerated oxygen evolution reaction

Yanan Li<sup>1</sup>, Ruopian Fang<sup>1</sup>, Jiangtao Xu<sup>1</sup>, Da-Wei Wang<sup>1,2,3</sup> and Lixue Jiang<sup>1</sup> on

Water electrolysis powered by renewable energy is recognized as a sustainable approach for green hydrogen production. Rational design of efficient and low-cost electrocatalysts especially for the sluggish oxygen evolution reaction (OER) remains a significant challenge. Here, we report a two-step surface reconstruction strategy, alkaline etching and anodic activation on CoAl hydroxide electrodes which remarkably enhance the OER performance. A low overpotential of 269 mV at 10 mA cm<sup>-2</sup> is achieved in 1 M KOH electrolyte, along with a notably reduced *Tafel slope* of 37 mV dec<sup>-1</sup>, a 16-fold enhanced catalyst intrinsic activity at an overpotential of 300 mV, and excellent stability without noticeable degradation over 50 hours operation. The dynamic surface reconstruction of CoAl hydroxide catalyst is evidenced by physical characterization in the process of alkaline etching and anodic activation. The defective structure and the modulated electronic distribution on the catalyst surface are demonstrated to facilitate electron transfer and OER kinetics. Our work presents a feasible surface reconstruction approach for designing high-efficiency catalytic electrodes in alkaline water electrolysis.

ith centuries of industrialization, the consumption of fossil fuels that formed millions of years ago continually causes greenhouse gases emission, leading to global warming and environmental pollution. The world requires affordable, accessible, and sustainable energy solutions to replace fossil fuels.[1] Water electrolysis is a sustainable approach to store intermittent renewable energy (e.g., solar and wind) in the form of chemical energy, that is green hydrogen with only pure water byproduct when combusted. Water electrolysis consists of two individual half-cell reactions hydrogen evolution reaction (HER) and oxygen evolution reaction (OER).[2] OER is the bottleneck of water electrolysis efficiency due to its involvement in a four-electron transfer process, which results in sluggish reaction kinetics and a higher overpotential compared to HER. Noble metalbased electrocatalysts, such as IrO2 and RuO2 have been recognized as efficient electrocatalysts for OER, but their scarcity, high cost, and poor stability have restricted the largescale implementation in developing a global green hydrogen economy. Thus, research on earth-abundant alternatives for OER catalysts has become imperative. However, developing non-noble electrocatalysts with balanced activity and stabil-

Received 23 January 2025; Accepted 17 June 2025; Published online 13 October 2025

ity for the sluggish OER presents a substantial challenge.

In recent years, transition metal-based OER electrocatalysts have been developed via various strategies, such as composition optimization, nano-size control, and phase regulation. [3-5] Among those, most of these strategies have primarily focused on modifying the bulk properties of the catalysts. Traditional bulk electrode materials are gradually approaching their performance limits due to the limited number of active sites and the deactivation effect. [6-7] In fact, the OER only occurs on the catalytic surface, and the catalytic performance depends on surface electronic structure, real electrochemical surface area, and interfacial charge transfer efficiency. [8-9] Hence, instead of modulating the bulk phase of the catalyst, surface reconstruction strategies are highly desirable for further improving the catalytic activity. [10]

Alkaline etching is an effective strategy to create vacancy defects and trigger surface reconstruction on the catalyst.<sup>[10]</sup> When introducing vacancy defects, the absence of atoms in the lattice site could expose the surrounding unsaturated metal sites and induce electron redistribution to balance the charge, leading to tuned electronic structure for fast charge transfer.<sup>[7,11–12]</sup> Kuang and Sun's group introduced base-soluble sites Zn<sup>2+</sup>/Al<sup>3+</sup> into NiFe LDHs followed by alkaline etching to selectively create coordination-unsaturated atomic defect, which expanded the electrochemical active surface area (*ECSA*), tuned the valence state of the active sites, eventually changed the determining step of OER rate and facilitated the OER kinetics.<sup>[12]</sup>

However, controlling the surface electronic structure of the catalyst at the band gap level is still a challenge. Electrochemical activation, including anodic activation, [13] cathodic activation, [14-17] and electrochemical aging, [18-22] etc., offers great

<sup>&</sup>lt;sup>1</sup> School of Chemical Engineering, University of New South Wales, Sydney, NSW 2052, Australia

<sup>&</sup>lt;sup>2</sup> Faculty of Materials Science and Energy Engineering, Shenzhen University of Advanced Technology, Shenzhen 518071, China

<sup>&</sup>lt;sup>3</sup> Institute of Technology for Carbon Neutrality, Shenzhen Institute of Advanced Technology, Chinese Academy of Sciences, Shenzhen 518071, China

 $<sup>*</sup> Corresponding \ author, E-mail: dawei.wang@siat.ac.cn; lixue.jiang@unsw.edu.au\\$ 

potentials for triggering surface reconstruction in a facile and controlled manner.<sup>[17]</sup> During anodic polarization, many transition metals based pre-catalysts undergo in situ surface reconstruction and are oxidized into more active oxyhydroxide species, which have been widely confirmed as the real active sites for OER. Inspired by this, researchers gained the real active phase via applying electrochemical activation.<sup>[10]</sup> Furthermore, electrochemical activation may change the surface electronic structure via leaching of some metal cations or anions, creating vacancies, defects and edges,<sup>[14,17,23]</sup> which expose more active sites and tune the intrinsic activity.

Among transition metal-based catalysts, cobalt-based oxides and (oxy)hydroxides have been widely applied as electrocatalysts for HER and OER in water splitting, owing to their adjustable valence states and tunable electronic structures, achieved by controlling the Co<sup>2+</sup>/Co<sup>3+</sup> ratio or introducing defects.[23-25] Soluble Al3+ sites can be introduced into the matrix and then selectively etched in a strong alkaline solution to create defects and cation vacancies within the matrix.[11-12] Herein, we report a two-step surface reconstruction strategy that combines alkaline etching and electrochemical activation to induce surface reconstruction of CoAl hydroxide deposited on nickel foam (NF). The in-situ surface reconstruction modulates electronic distribution and tunes the active sites on the ultrathin nanofilm, thereby enhancing intrinsic activity and accelerating OER kinetics. The activated CoAl/NF exhibits a low OER overpotential of 269 mV at 10 mA<sup>-2</sup> in 1 M KOH electrolyte, a superior Tafel slope of 37 mV dec<sup>-1</sup> and enhanced intrinsic catalytic activity. The activated CoAl/NF is also found to be highly stable in both long-term chronopotentiometry (CP) and cyclic voltammetry (CV) evaluation.

#### **Results and discussion**

Figure 1 outlines the two-step surface reconstruction process of a CoAl hydroxide electrode and Figure S1 shows the corresponding OER performance. In the first step, defect-containing CoAl hydroxide (D-CoAl/NF) was prepared by electrodepositing Co<sup>2+</sup>Al<sup>3+</sup>(OH)<sub>x</sub> nanosheets onto NFs, followed by alkaline etching of the dissolvable Al<sup>3+</sup> sites to create vacancy defects in the CoAl hydroxide lattice. The second step involves the preparation of activated CoAl hydroxide (A-CoAl/NF) by repetitively applying anodic linear sweep voltam-

metry (LSV). The polarization curve shifts dramatically to a lower potential after the first LSV process and continues to improve with the subsequent LSVs until it becomes stable. After anodic activation, the color of the catalyst changes from metallic grey to a slightly darker shade of metallic gray (Figure S2). The electrodeposited CoAl/NF, alkaline etched CoAl/NF, and anodic activated CoAl/NF catalysts are denoted as CoAl/NF, D-CoAl/NF and A-CoAl/NF, respectively.

Defect-rich structures typically enhance catalytic activity by tunning electronic structure, but alkaline etching may damage the original structure and thus reduce the catalyst activity, so it is important to determine the appropriate Co/Al ratio and etching conditions. A series of experiments (Figure S3-6) were conducted to determine the optimal Co/Al ratio of the electrodeposition electrolyte (Co<sub>1</sub>Al<sub>0.5</sub>), etching concentration (5M NaOH solution), and etching time (30 minutes). We performed characterization analysis under the optimized experimental parameters.

The comparison of the structural characterization between pristine CoAl/NF and Co(OH)<sub>2</sub>/NF (Figure S7-8) demonstrates the successful deposition of Co<sup>2+</sup>Al<sup>3+</sup>(OH), nanosheets onto the NF substrate. In contrast to Co(OH)2/NF, which exhibits a two-dimensional hydrotalcite-like nanosheet structure under the scanning electron microscopy (SEM), the pristine CoAl/NF displays a thinner nanosheet morphology (Figure S7a-b). Energy-dispersive X-ray spectroscopy (EDS) elemental mapping of CoAl/NF indicates homogeneous distribution of four major elements Ni, Co, Al, and O across the entire sample (Figure S7d). The X-ray diffraction (XRD) patterns (Figure S7c) primarily display strong peaks from the NF substrate, with no distinct peaks corresponding to the CoAl layer. This can be attributed either to the amorphous state of the electrodeposited catalysts[11] or to the CoAl layer being too thin to detect, due to the low deposition current and low electrolyte concentration used during electrodeposition. X-ray photoelectron spectroscopy (XPS) further confirms the deposition of Al. The Al 2p XPS spectrum of the CoAl/NF shows peak located at 74.2 eV, which can be assigned to trivalent aluminum (Figure S8).[26] XPS analysis of Co 2p of CoAl/NF reveals no shifts in the binding energy of the components corresponding to Co(OH)<sub>2</sub>/NF, suggesting negligible electronic modification when replacing part of the Co-host lattice with Al sites.

Characterization analyses were conducted to investigate

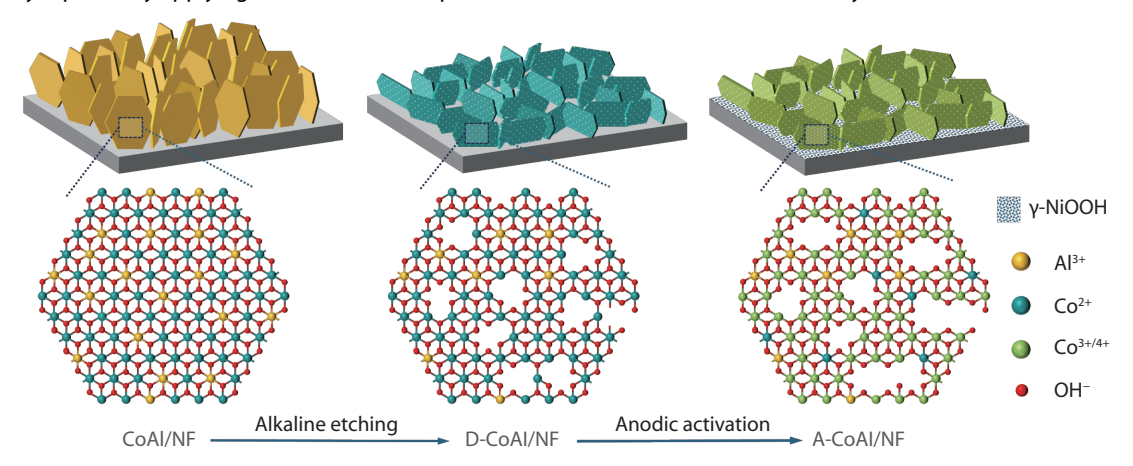


Fig. 1 Schematic illustrations of the synthesis of A-CoAl/NF.

the alkaline etching process. SEM was performed to investigate the evolution of surface morphology before and after alkaline etching (Figure 2a-b). Compared with the pristine CoAl/NF, D-CoAl/NF features thinner nanosheets morphology. Al atomic ratios determined from the XPS reveals that the D-CoAl/NF (Al at%=12.3) contains evidently less Al<sup>3+</sup> compared with CoAl/NF (Al at%=35.2), demonstrating selective alkaline etching successfully removal partial Al<sup>3+</sup> sites (Figure 2d). This result aligns with the previous optimal etching concentration experiment where the Al atomic ratio of the etched catalysts decreases with the increasing alkalinity of the NaOH solution experiment (Figure S5b). As amphoteric compound, aluminum hydroxide can react with hydroxide ions to form soluble Al(OH)<sub>4</sub><sup>-</sup> (Equation S1), leaving Al<sup>3+</sup> vacancy in the CoAl hydroxide lattice.

Furthermore, the changes of valence state shown by XPS correlate well with the defect characteristics. After alkaline etching, both the Co 2p and Al 2p XPS binding energy of D-CoAl/NF shifts 0.2 eV to a lower position (Figure 2e-f). Defects created by leaching Al³+ from laminates should expose the surrounding unsaturated cation sites. As the electron withdrawing power coming from Al³+ sites disappeared, electrons move to the surrounding metal sites to balance the charge of the leaving groups. Thus, the surrounding metal sites negatively shift to a lower valence state to balance the charge of the cation vacancy.[11-12] We also conducted characterization analysis on Ni species. Ni 2p/3 XPS Spectrum of CoAl/NF is curve fitted into three peaks located at 852.6 eV, 853.7 eV and 855.8 eV, corresponding to Ni metal, NiO, Ni(OH)<sub>2</sub>, respectively.<sup>[27-29]</sup> After alkaline etching, the Ni 2p XPS spectrum

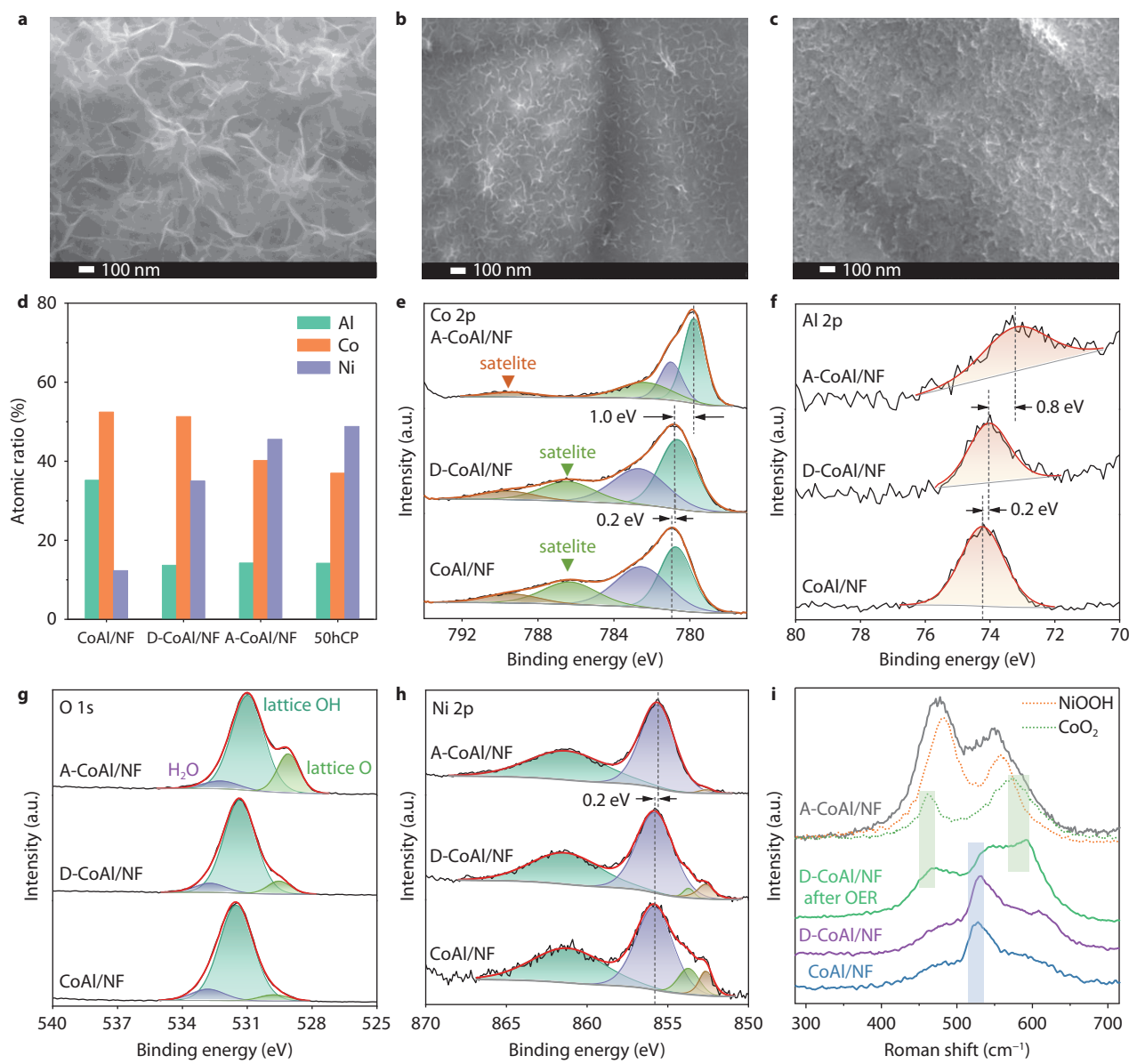


Fig. 2 Characterization analysis of CoAl/NF, D-CoAl/NF and A-CoAl/NF. SEM images of a CoAl/NF, b D-CoAl/NF, c A-CoAl/NF. d Co, Ni, Al atomic ratio (Co at% + Ni at% + Al at% = 100%). High-resolution XPS of CoAl/NF, D-CoAl/NF and A-CoAl/NF e Co 2p, f Al 2p, g O 1s, h Ni 2p. i Ex situ Raman spectra.

shows an improved signal-to-noise ratio compared to CoAl/NF, indicating an enhanced Ni signal on the film (Figure 2h).

Based on the above characterization, the etching process can be explained as follows. During alkaline etching, Al3+ species in the CoAl/NF are selectively leached out, creating Al3+ cation vacancies in the Co<sup>2+</sup>Al<sup>3+</sup>(OH)<sub>x</sub> nanosheets. This selective removal also disrupts the coordination environment of adiacent Co<sup>2+</sup> sites, leading to the detachment of some Co<sup>2+</sup> sites from the CoAl nanosheet lattice. As a result, the upper portion of the nanosheets peels off, while the CoAl layers become thinner but remain strongly adhered to the NF substrate (Figure 1). The SEM image of D-CoAl/NF (Figure 2b) indicates a thinner nanosheet layer and the appearance of a blue color in the etching solution (Figure S4b) indicates the leaching of Co(OH)<sub>2</sub>. It is noteworthy that the leaching of Al does not directly expose Ni sites from the substrate, but through thin the nanolayer to make the Ni signal is easy to detect by XPS. Moreover, thinner nanolayer benefit the OER performance of catalyst. The ultrathin materials provides a favourable environment for the formation and evolution of various types of defects which can tune the electronic structure and enhance performance.[7,30-32] The residual CoAl nanosheets maintain strong adhesion to the NF substrate, which contributes to improved structural stability.

Characterization analyses were also conducted to investigate the following anodic activation process. The surface of A-CoAl/NF performed by SEM (Figure 2c) shows an embossed morphology, indicative of surface reconstruction during anodic activation process. As a surface analysis tool, XPS can help to better understand the surface reconstruction including the composition and valence state change caused by anodic activation. The spectral fitting parameters of the curve fitted Co 2p3/2 XPS spectrum in both CoAl/NF and D-CoAl/NF (Figure 2e) match with XPS analysis of the pure Co(OH)<sub>2</sub>, [28,33] revealing the predominant species are mainly Co2+. This also correlate well with the electrodeposition reactions (Equation S2-3).[34-36] However, after anodic activation, Co 2p XPS spectrum of A-CoAl/NF exhibits characteristic peaks of a higher oxidation state (Figure 2e). The satellite peak decreases significantly accompanied by a change in its position, which can be used to identity the Co<sup>3+</sup> and higher oxidation states.<sup>[23,37]</sup> The Co 2p XPS spectrum significantly shifts 1.0 eV to a lower binding energy of 779.8 eV, further confirming that the Co species in A-CoAl/NF has transitioned to a higher oxidation state, because the peak of CoOOH, Co<sub>3</sub>O<sub>4</sub> and CoO<sub>2</sub> are all lower than the peak of Co(OH)<sub>2</sub>.[38-40] The above analyses also align well with Pourbaix diagrams of cobalt[41] and electrochemical knowledge. During the electrochemical anodic scan, Co(OH)<sub>2</sub> is first converted to the active species CoOOH (Equation S4). With the anodic potential increases, the CoOOH partially transforms into CoO<sub>2</sub> (Equation S5), which has also been proposed as the active OER species in previous studies on cobalt oxides.[42-44] The deconvoluted peaks O1s XPS spectrum of the D-CoAl/NF at 529.5, 531.3, 532.8 eV are assigned to lattice O, lattice OH, and the adsorbed H<sub>2</sub>O, respectively (Figure 2g). After anodic activation, the significant growth of the lattice O peak that related to the lattice oxide in the M-O or M-OOH also indicates the formation of CoOOH/CoO<sub>2</sub>. [29,45-48]

Meanwhile, we notice that the main peak of Al 2p in A-

CoAl/NF further shifts by 0.8 eV, approaching the position of metallic Al (Figure 2f). The main peak of Ni 2p in A-CoAl/NF also shifts 0.2 eV to a lower binding energy of 855.6 eV. According to the electrochemical knowledge,  $\alpha$ -Ni(OH)<sub>2</sub> will be oxidized to  $\gamma$ -NiOOH when applying electrochemical anodic scan (Equation S6), and  $\beta$ -NiOOH can also be converted to  $\gamma$ -NiOOH when the applied electrochemical potential exceeds 0.6V (vs Hg/HgO).<sup>[21,49]</sup> In our work, considering that the LSV potential applied to the catalyst reaches 0.9 V (vs. Hg/HgO), the active Ni species are expected to be primarily  $\gamma$ -NiOOH.

The CoAl/NF and D-CoAl samples were investigated by Raman spectroscopy under dry conditions, and the activated samples were investigated by Raman spectroscopy under wet conditions right after the OER electrochemical test (Figure 2i). For CoAl/NF and D-CoAl/NF samples, the highly polarized band at 528 cm<sup>-1</sup> is attributed to the Co-O ( $A_a$ ) stretching mode of Co(OH)<sub>2</sub>.[50] After the first anodic scan, two new peaks at 466 and 592 cm<sup>-1</sup> appeared, which are assigned to the  $A_{1a}$  and  $E_a$  vibrational modes of  $CoO_{2}$ , [51] indicating the conversion of Co(OH)<sub>2</sub> to CoO<sub>2</sub> during anodic activation. Further spectral changes were observed for the fully activated sample: two board spectral features around 475 and 550 cm<sup>-1</sup>. To further investigate this proposal, Co(OH)<sub>2</sub>/NF and NF were etched and activated by the same process as A-CoAl/NF, and their crystal structures were investigated by Raman spectroscopy. The peaks at 461 and 574 cm<sup>-1</sup> for the activated Co(OH)<sub>2</sub>/NF match that of disordered CoO<sub>2</sub> species,<sup>[52]</sup> indicating the activated samples contains a large portion of CoO<sub>2</sub>, probably in a mixture with CoOOH that is invisible in the Raman spectrum. For the activated NF sample, the Raman bonds at 480 and 557 cm<sup>-1</sup> with an intensity ratio ( $I_{479}/I_{557}$ ) of 1.4 suggests a signal of  $\gamma$ -NiOOH phase.<sup>[18,21,53]</sup> The Raman peaks of CoO<sub>2</sub> and γ-NiOOH are quite close to each other, thus we propose that the broad Raman band of A-CoAl/NF is comprised of a mixture of γ-NiOOH and disordered CoO<sub>2</sub> species spectroscopy signals.

Thus far, our findings indicate that two main changes occur during anodic activation. On one hand,  $Co(OH)_2$  and  $Ni(OH)_2$  undergo electrochemical oxidation to tune  $CoOOH/CoO_2$  and  $\gamma$ -NiOOH active sites. It is known that, when the metal cations in the catalyst surface are oxidized into the higher valence, the high valence state active sites are unsteady and incomplete. Through repeatedly anodic activation, the unsteady and incomplete active sites can be transformed into stable and complete active sites, which dynamically enhance the crystallinity of the active sites and tune the active sites. The presence of peaks in K 2p spectra (Figure S9) could demonstrate this deduction. The K+ ions from the KOH electrolyte intercalates into the interlayer space of  $\gamma$ -NiOOH and CoOOH during anodic activation process, leading to layer contraction that helps to improve the activity. [18] [55]

On the other hand, the main peak of Co 2p, Al 2p and Ni 2p all display evident negative shift, by 1.0 eV, 0.8 eV and 0.2 eV, respectively, causing strong electronic redistribution on the surface of the catalyst. It is different from common knowledge that the negative shift of XPS peak indicates a reduced oxidation state. In the case of Co 2p, the peak of CoOOH, Co<sub>3</sub>O<sub>4</sub> and CoO<sub>2</sub> usually appear at lower binding energies than that of Co(OH).<sup>[23,33,38-40]</sup> This is because the binding energy is not always related solely to the electronegativity of the

surrounding elements but also depend on the overall electronic environment of the lattice.<sup>[56]</sup> According to the current reports, the negative binding energy shifts of the cation metals usually come along with defective structure.<sup>[12,17,57]</sup> With the decreasing binding energy of the cation metals, electrons move to the cation sites, causing structural disorder such as edges and defects, which further enhance the unsaturated electronic structure on the defective catalytic surface. By applying repetitive anodic linear sweep voltammetry (LSV), Co hydroxides are oxidized into a higher oxidation valence CoOOH/CoO<sub>2</sub>, which possesses a lower binding energy than Co hydroxide, leading to the electrons move to cation metals, further enhancing the unsaturated electronic structure on the defective catalytic surface.

Based on the OER mechanism, the binding strengths between the active sites and the oxygen-containing intermediates (\*OH, \*O and \*OOH, where \* refers to the active site on the electrocatalyst) should not be too strong or too weak to ensure a balance between the adsorption and desorption. The unsaturated electronic structure adjusts the electron configuration on the catalytic surface, modulates the binding strengths of reaction intermediates, and alters their adsorption/desorption energies. This adjustment lowers the energy barriers for the oxygen evolution reaction (OER) and enhances electron transfer efficiency.<sup>[58-60]</sup> This deduction is further validated by electrochemical impedance spectroscopy measurements, which show that the charge transfer resistance (Rct) decreases in parallel with the overpotential during anodic activation process (Figure 3a-b). Given the OER process is dominantly controlled by the charge transfer process under low current conditions, a low charge transfer resistance can effectively boost OER kinetics.[61] In addition, the ultrathin catalyst film also benefits the electron transfer. During anodic activation process, the intensity of the redox peak did not increase obviously, meaning the catalyst films didn't evidently thicken.<sup>[21,62]</sup> As it has been found that catalyst films with a thickness of 1 to 2 nm are sufficient to exhibit catalytic performance in low current densities applications, while a thick oxidation film could cause damage to the catalyst activity by impeding the electron transfer from surface active sites to inner matrix.<sup>[18,55]</sup>

Apart from this, Co(OH)<sub>2</sub>/NF was etched and activated by the same process as A-CoAl/NF to further investigate activation mechanism. The results show that A-Co(OH)<sub>2</sub>/NF exhibits lower OER activity compared to A-CoAl/NF (Figure 3c). As shown in XPS analysis (Figure S10a), the negative shift of Co 2p due to anodic activation (0.3 eV) in A-Co(OH)<sub>2</sub>/NF is significantly smaller than the 1.0 eV shift observed in A-CoAl/NF. This supports the previous explanation that the enhanced activity of A-CoAl/NF is attributed to strong electronic redistribution. The A-Co(OH)<sub>2</sub>/NF exhibits lower CV stability compared to A-CoAl/NF (Figure 3c-e). Typically, CV is conducted to achieve a stable polarization current before measuring LSV. A-CoAl/NF is easy to achieve a stable polarization current when applying CV scan, while A-Co(OH)<sub>2</sub>/NF deteriorates continuously until the performance reverts to its non-activated value. Compared to A-CoAl/NF, the Co atomic ratio in A-Co(OH)<sub>2</sub>/NF drops significantly after anodic activation (Figure S10a) and the lattice oxygen peak associated with CoOOH nearly disappears (Figure S10b), indicating the electrocatalytic instability of A-Co(OH)<sub>2</sub>/NF is caused by dissolution of Co active sites during operation. [63-64] We infer that the Al3+ cation vacancies benefit the stability of the catalyst by preventing Co dissolution. This aligns with findings in the literat-

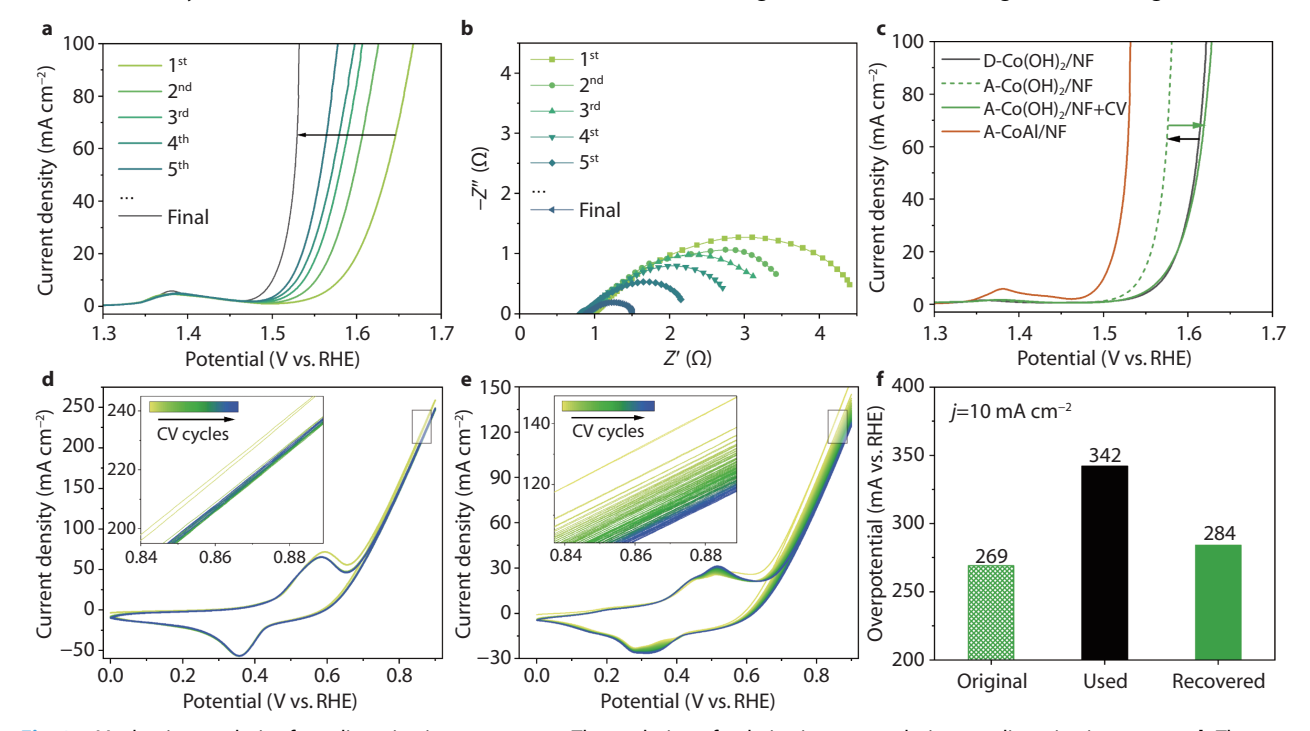


Fig. 3 Mechanism analysis of anodic activation processes. **a** The evolution of polarization curves during anodic activation process. **b** The corresponding Nyquist plots with the LSV polarization curves in **a**. **c** Polarization curves of A-Co(OH)<sub>2</sub>/NF before and after CVs. CV curves and its zoom-in image of **d** A-CoAl/NF and **e** A-Co(OH)<sub>2</sub>/NF. **f** The overpotential of original, used and recovered A-CoAl/NF.

ure, which indicate that cation vacancy defects not only enhance the activity of electrocatalysts but also improve their stability. [65–66] Waterhouse et al. demonstrated that the cation vacancies contribute to stability of NiFe-LDH catalysts by strengthening the binding energy of \*O bond and release lattice distortion, thus suppressing metal sites dissolution and enhance the OER stability. [67]

To further understand the role of nickel in the OER performance of CoAl/NF, NF was etched and activated by the same process as A-CoAl/NF. The result shows that, A-NF exhibited an overpotential of 328 mV at 10 mA cm<sup>-2</sup>, which is considerably higher than that of A-CoAl/NF (Figure S11). This indicates that, without the contribution of the defective CoAl nanolayer, the nickel active sites alone cannot achieve the catalytic activity of 269 mV at 10 mA cm<sup>-2</sup>. This is consistent with the etching experiments shown in Figure S5, where the best performance was not achieved with 6 M NaOH which would expose more Ni, but rather with 5 M NaOH. This is because over-leaching of Al3+ disrupts the Co2+ network, reducing the number of active Co sites and harming catalytic performance. These findings indicate that the defective CoAl nanolayer plays a more critical role in OER performance than the Ni sites. We know that Co is considered less active than Ni or Fe for OER. However, catalyst performance is not determined solely by the type of active sites, as it cannot explain why different catalysts with the same active sites and oxidation states exhibit significantly different OER activities. The activity of the catalyst also depends on the surface electronic structure, influence the binding strength of intermediates \*OH, \*O, and \*OOH, which in turn influence the rate determining step of the OER, thereby enhancing the overall reaction kinetics. [58–60] Thus, Co-based materials can achieve high OER activity when their surface structure is properly tuned.

In addition, as the Co/Al ratio of A-CoAl/NF is approximately 3:1 (as shown in Figure 2d), we compared the catalytic performance of a catalyst directly synthesized with a 3:1 Co/Al ratio (Co<sub>1</sub>Al<sub>0.33</sub>/NF) to that of the activated sample (A-CoAl/NF) to demonstrate the overall effect of the activation process. As shown in Figure S12, the OER performance of Co<sub>1</sub>Al<sub>0.33</sub>/NF is significantly lower than that of A-CoAl/NF, highlighting the critical role of surface reconstruction in enhancing catalytic activity.

Furthermore, we attempted to recover the used A-CoAl/NF electrode that had been stored in the air for a week. Remarkably, we observed that the used electrode could be reactivated by reapplying anodic activation, with the overpotential returning to a value close to its original level (Figure 3f, S13). The results indicate that the in-situ reconstruction is repeatable, enabling A-CoAl/NF to function as a self-healing electrode for OER applications, which is beneficial for practical use

We evaluated the OER performance of the A-CoAl/NF under the optimized experimental parameters. For comparison, pristine CoAl/NF, Co(OH)<sub>2</sub>/NF were also evaluated. Figure 4a-b shows that A-CoAl/NF displays excellent OER catalytic performance, with the overpotentials as low as 269 mV at a current density of 10 mA cm<sup>-2</sup>, much lower than those of the pristine CoAl/NF (338 mV@10 mA cm<sup>-2</sup>) and Co(OH)<sub>2</sub>/NF (313 mV@10 mA cm<sup>-2</sup>). As shown in Figure 4c, the A-CoAl/NF displays a much smaller *Tafel slope* (37 mV dec<sup>-1</sup>) compared with

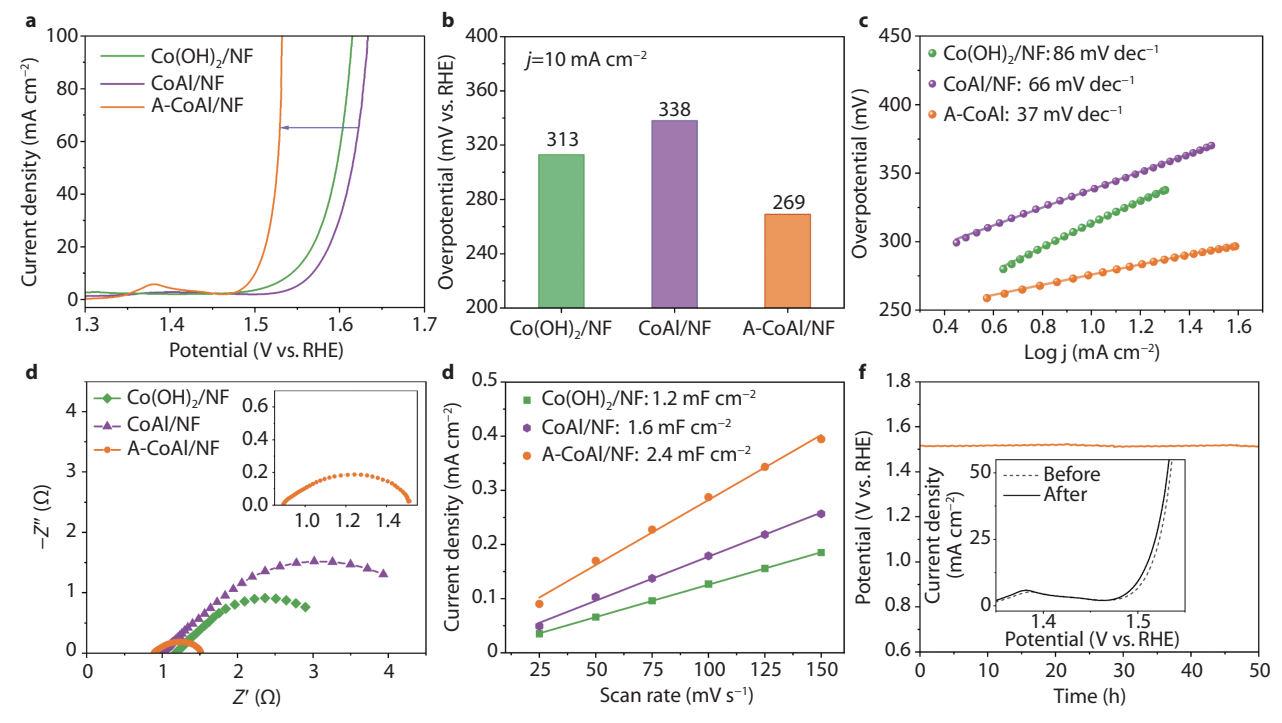


Fig. 4 Electrocatalytic OER performance of A-CoAl/NF and reference samples. **a** Polarization curves of A-CoAl/NF in 1 M KOH, with that of  $Co(OH)_2/NF$ , and CoAl/NF for comparison. **b** Comparison of overpotentials required for current density j = 10 mA. **c** The corresponding Tafel plots. **d** The corresponding Nyquist plots. **e** The corresponding double-layer capacitance measurements ( $C_{dl}$  values). **f** Chronopotentiometry curves of A-CoAl/NF at constant current densities of 10 mA cm<sup>-2</sup>, inset: OER performance before and after 50h CP test.

the pristine CoAl/NF (66 mV dec<sup>-1</sup>) and the Co(OH)<sub>2</sub>/NF (86 mV dec<sup>-1</sup>), indicating superior OER kinetics for the activated electrode. The low overpotential and small *Tafel slope* value of A-CoAl/NF electrode are superior to the commercial IrO<sub>2</sub> catalysts, and comparable to or even better than state-of-the-art OER catalysts (Table S1). The significantly reduced *Tafel slope* suggests that the rate determining step in electron transfer mechanism has changed. A *Tafel slope* close to 40 mV dec<sup>-1</sup> implies that \*O bond formation during the second electron transfer is rate determining step.<sup>[54,68–69]</sup> The etching and activation processes induce electronic redistribution on the catalyst surface, altering the bonding energy of oxygen-containing intermediates. This modification changes the rate-determining step of the oxygen evolution reaction (OER), thereby enhancing OER kinetics.

Nyquist plots of the electrocatalysts show that A-CoAl/NF displays the lowest  $R_{ct}$  (0.6  $\Omega$ ) compared with the other two electrocatalysts, indicating the etching and activation process facilitates charge transfer (Figure 4d). The double-layer capacitance ( $C_{dl}$ ) was measured to gain insight into the ECSA of the catalyst (Figure 4e and Figure S14a-c). The A-CoAl/NF exhibits a higher  $C_{dl}$  value (2.4 mF cm<sup>-2</sup>) compared to its pristine catalyst (1.6 mF cm<sup>-2</sup>), indicating an increased ECSA. This enhancement is attributed to the defective electronic structure caused by the etching and activation process. Moreover, by normalizing the OER current to ECSA at  $\eta$  =300mV, the A-CoAl/NF demonstrates significantly high intrinsic activity (1.73 mA cm<sup>-2</sup> ECSA), approximately 16 times greater than that of the pristine catalyst and 5 times higher than that of Co(OH)<sub>2</sub>/NF (Figure S14d-f).

To assess the electrocatalytic stability of A-CoAl/NF toward OER, CP stability test was conducted at a current density of 10 mA cm<sup>-2</sup> for 50 hours (Figure 4f). The A-CoAl/NF exhibits robust stability with no degradation in the OER performance after stability test. The XPS analysis reveals negligible changes in element ratios and valence states after the stability test (Figure 2d, S15). The inset is the polarization curves of A-CoAl/NF before and after 50 hours CP test, showing the OER performance becomes even better after the stability test, indicating a dynamically self-optimized trend of the electrode. It's worth noting that, although the OER occurs in an alkaline environment, no Al leaching was observed in the A-CoAl/NF electrode during prolonged OER operation. The XPS analysis (Figure 2d) confirm that the Al content remains unchanged even after a 50-hour CP test at a constant current density of 10 mA cm<sup>-2</sup>. The stability of Al can be explained as follows. The concentration of the alkaline etching solution used in this study is 5 M, which is significantly higher than that of the 1 M KOH electrolyte used during the OER test. This higher alkalinity facilitates the reaction of aluminum hydroxide with hydroxide ions to form soluble Al(OH)<sub>4</sub>-, enabling its removal from the CoAl hydroxide lattice during the etching process. In contrast, the milder alkaline environment during OER cannot promote further Al leaching. Additionally, the A-CoAl/NF electrode undergoes repeated anodic activation for up to 10 hours. During this process, the surface electronic structure experiences continuous reconstruction and gradually reaches a stable state under OER alkaline conditions. As a result, the remaining Al sites are strongly integrated into the structure and exhibit high resistance to leaching during additional longterm OER operations.

#### **Conclusion**

In summary, a unique activation strategy involving alkaline etching and anodic activation was employed to trigger in-situ surface reconstruction of A-CoAl/NF, dramatically boosting the OER activity in alkaline media. The activated catalyst reguires a reduced overpotential of 269 mV to deliver the current density of 10 mA cm<sup>-2</sup>, along with superior catalytic kinetics with a small Tafel slope of 37 mV dec-1, high intrinsic activity by normalizing the OER current to ECSA, and high stability in both CV and CP evaluation. Through comprehensive characterization, we demonstrate that alkaline etching introduces aluminum vacancies in CoAl hydroxide electrodes. Subsequent anodic activation further modulates the electronic configuration of the unsaturated structure, thereby reducing the energy barriers for the oxygen evolution reaction and facilitating electron transfer kinetics. Meanwhile, anodic activation dynamically tunes the CoOOH/CoO<sub>2</sub> and γ-NiOOH active sites and enhances the intrinsic activity. This work provides a new activation strategy to boost the OER performance of non-noble catalysts in alkaline medium, gains an important insight for understanding the dynamic in situ reconstruction of catalyst under anodic activation, and offers creative inspiration for further research on electrocatalyst activation.

#### ACKNOWLEDGMENTS

The authors acknowledge the scientific and technical assistance from the assistance from the Microscopy Australia at the Electron Microscope Unit (EMU), the Solid State & Elemental Analysis Unit (SSEAU) and Spectroscopy Laboratory (SPECLAB) within the Mark Wainwright Analytical Centre (MWAC) at UNSW Sydney. This work was financially supported by the Australian Research Council Discovery Early Career Researcher Award (DE210101157), Discovery Project (DP190101008, DP220102436), **Future Fellowship** (FT190100058), and University of New South Wales/Chinese Academy of Sciences Collaborative Research Seed Program.

#### CONFLICT OF INTEREST

The authors declare no conflict of interest.

## **■ AUTHOR CONTRIBUTIONS**

Lixue Jiang and Da-Wei Wang conceived the concept and supervise the research. Yanan Li conducted experiments and wrote the manuscript. Lixue Jiang and Ruopian Fang revised the manuscript. All authors contributed to the discussion of the manuscript.

### REFERENCES

- 1. S. Chu, A. Majumdar, *Nature*, 2012, 488, 294
- M. Wang, Z. Wang, X. Gong, Z. Guo, Renew. Sust. Energ. Rev., 2014, 29, 573
- W. Wang, Y. Liu, S. Chen, Acta Physico-Chimica Sinica, 2024, 40, 2303059
- 4. J. Ding, D. Zhang, A. Riaz, H. Gu, J. Z. Soo, P. R. Narangari, C.

- Jagadish, H. H. Tan, S. Karuturi, CCS Chemistry, 2024, 6, 2692
- 5. N. Wen, X. Jiao, Y. Xia, D. Chen, *Mater. Chem. Front.*, 2023, 7, 4833
- F. Zeng, C. Mebrahtu, L. Liao, A. K. Beine, R. Palkovits, J. Energy Chem., 2022, 69, 301
- 7. F. Liu, Z. Fan, Chem. Soc. Rev., 2023, 52, 1723
- Z. Kou, X. Li, L. Zhang, W. Zang, X. Gao, J. Wang, Small Sci., 2021, 1, 2100011
- L. Wu, Z. Guan, D. Guo, L. Yang, X. a. Chen, S. Wang, Small, 2023, 19, 2304007
- L. Gao, X. Cui, C. D. Sewell, J. Li, Z. Lin, *Chem. Soc. Rev.*, 2021, 50, 8428
- H. Li, L. Zhang, S. Wang, J. Yu, Int. J. Hydrog. Energy, 2019, 44, 28556
- 12. Q. Xie, Z. Cai, P. Li, D. Zhou, Y. Bi, X. Xiong, E. Hu, Y. Li, Y. Kuang, X. Sun, *Nano Res.*, 2018, 11, 4524
- H. Jiang, Q. He, X. Li, X. Su, Y. Zhang, S. Chen, S. Zhang, G. Zhang,
  J. Jiang, Y. Luo, P. M. Ajayan, L. Song, *Adv. Mater.*, 2019, 31, 1805127
- P. Guo, S. Cao, Y. Wang, X. Lu, Y. Zhang, X. Xin, X. Chi, X. Yu, I. Tojiboyev, H. Salari, A. J. Sobrido, M. Titirici, X. Li, *Appl. Catal. B*, 2022, 310, 121355
- G. R. Zhang, L. L. Shen, P. Schmatz, K. Krois, B. J. M. Etzold, *J. Energy Chem.*, 2020, 49, 153
- K. Wu, F. Chu, Y. Meng, K. Edalati, Q. Gao, W. Li, H. J. Lin, J. Mater. Chem. A., 2021, 9, 12152
- B. Dong, M. -X. Li, X. Shang, Y. N. Zhou, W. H. Hu, Y. M. Chai, J. Mater. Chem. A., 2022, 10, 17477
- J. Huang, Y. Li, Y. Zhang, G. Rao, C. Wu, Y. Hu, X. Wang, R. Lu, Y. Li, J. Xiong, *Angew. Chem. Int. Ed.*, 2019, 131, 17619
- 19. H. Bode, K. Dehmelt, J. Witte, Z. Anorg. Allg. Chem., 1969, 366, 1
- 20. F. Dionigi, P. Strasser, *Adv. Energy Mater.*, 2016, 6, 1600621
- 21. B. S. Yeo, A. T. Bell, J. Phys. Chem. C., 2012, 116, 8394
- S. L. Medway, C. A. Lucas, A. Kowal, R. J. Nichols, D. Johnson, J. Electroanal. Chem., 2006, 587, 172
- 23. H. Huang, C. Yu, H. Huang, C. Zhao, B. Qiu, X. Yao, S. Li, X. Han, W. Guo, L. Dai, J. Qiu, *Nano Energy*, 2019, 58, 778
- Z. Cai, Y. Bi, E. Hu, W. C. Liu, N. S. Dwarica, Y. Tian, X. Li, Y. Kuang, Y. Li, X. Q. Yang, H. Wang, X. Sun, *Adv. Energy Mater.*, 2018, 8, 1701694
- L. Xu, Q. Jiang, Z. Xiao, X. Li, J. Huo, S. Wang, L. Dai, *Angew. Chem. Int. Ed.*, 2016, 55, 5277
- R. Zhang, C. Tang, R. Kong, G. Du, A. M. Asiri, L. Chen, X. Sun, *Nanoscale*, 2017, 9, 4793
- M. C. Biesinger, L. W. M. Lau, A. R. Gerson, R. S. C. Smart, *Phys. Chem. Chem. Phys.*, 2012, 14, 2434
- 28. M. C. Biesinger, B. P. Payne, A. P. Grosvenor, L. W. M. Lau, A. R. Gerson, R. S. C. Smart, *Appl. Surf. Sci.*, 2011, 257, 2717
- B. Payne, M. Biesinger, N. McIntyre, J. Electron. Spectrosc. Relat. Phenom., 2009, 175, 55
- 30. F. Song, X. Hu, *Nat. Commun.*, 2014, 5, 4477
- 31. F. Song, X. Hu, J. Am. Chem. Soc., 2014, 136, 16481
- H. S. Jadhav, A. Roy, B. Z. Desalegan, J. G. Seo, Sustain. Energy Fuels, 2020, 4, 312
- J. Yang, H. Liu, W. N. Martens, R. L. Frost, J. Phys. Chem. C., 2010, 114, 111
- F. Nasirpouri, Electrodeposition of Nanostructured Materials, Springer International Publishing AG, Germany, 2017.
- M. Shao, R. Zhang, Z. Li, M. Wei, D. G. Evans, X. Duan, *Chem. Commun.*, 2015, 51, 15880
- D. Zhou, P. Li, X. Lin, A. McKinley, Y. Kuang, W. Liu, W. F. Lin, X. Sun, X. Duan, Chem. Soc. Rev., 2021, 50, 8790
- 37. N. McIntyre, M. Cook, *Anal. Chem.*, 1975, 47, 2208
- 38. X. Wang, Y. He, Y. Zhou, R. Li, W. Lu, K. Wang, W. Liu, *Int. J. Hydrog. Energy*, 2022, 47, 23644
- M. Duraivel, S. Nagappan, K. H. Park, K. Prabakar, *Electrochim. Acta*, 2022, 411, 140071
- Y. Han, S. Axnanda, E. J. Crumlin, R. Chang, B. Mao, Z. Hussain, P. N. Ross, Y. Li, Z. Liu, *J. Phys. Chem. B*, 2018, 122, 666
- 41. M. Bajdich, M. García-Mota, A. Vojvodic, J. K. Nørskov, A. T. Bell, J.

- Am. Chem. Soc., 2013, 135, 13521
- 42. Y. -C. Liu, J. A. Koza, J. A. Switzer, *Electrochim. Acta*., 2014, 140, 359
- T. E. Rosser, J. P. S. Sousa, Y. Ziouani, O. Bondarchuk, D. Y. Petrovykh, X. K. Wei, J. J. L. Humphrey, M. Heggen, Y. V. Kolen'Ko, A. J. Wain, Catal. Sci. Technol., 2020, 10, 2398
- 44. A. Sivanantham, P. Ganesan, A. Vinu, S. Shanmugam, ACS Catal., 2020, 10, 463
- A. Moysiadou, S. Lee, C. S. Hsu, H. M. Chen, X. Hu, J. Am. Chem. Soc., 2020, 142, 11901
- N. Weidler, J. Schuch, F. Knaus, P. Stenner, S. Hoch, A. Maljusch, R. Schäfer, B. Kaiser, W. Jaegermann, J. Phys. Chem. C., 2017, 121, 6455
- D. Delgado, M. Minakshi, D. J. Kim, C. Kyeong W, Anal. Lett., 2017, 50, 2386
- 48. C. W. Hu, Y. Yamada, K. Yoshimura, *J. Mater. Chem. C*, 2016, 4, 5390
- S. R. Mellsop, A. Gardiner, B. Johannessen, A. T. Marshall, *Electrochim. Acta*, 2015, 168, 356
- H. B. Li, P. Liu, Y. Liang, J. Xiao, G. W. Yang, RSC Advances, 2013, 3, 26412
- Z. Chen, L. Cai, X. Yang, C. Kronawitter, L. Guo, S. Shen, B. E. Koel, *ACS Catal.*, 2018, 8, 1238
- N. Kornienko, N. Heidary, G. Cibin, E. Reisner, *Chem. Sci.*, 2018, 9, 5322
- 53. Y. L. Lo, B. J. Hwang, Langmuir, 1998, 14, 944
- Z. Qiu, C. W. Tai, G. A. Niklasson, T. Edvinsson, Energy Environ. Sci., 2019, 12, 572
- D. Tyndall, M. J. Craig, L. Gannon, C. McGuinness, N. McEvoy, A. Roy, M. García-Melchor, M. P. Browne, V. Nicolosi, *J. Mater. Chem.* A., 2023, 11, 4067
- J. M. Wagner, X-ray photoelectron spectroscopy, Nova Science Publishers, United States, 2011.
- X. Bo, Y. Li, R. K. Hocking, C. Zhao, ACS Appl. Mater. Interfaces, 2017, 9, 41239
- Q. Liang, L. Zhong, C. Du, Y. Luo, J. Zhao, Y. Zheng, J. Xu, J. Ma, C. Liu, S. Li, Q. Yan, ACS Nano, 2019, 13, 7975
- Y. I. Wang, T. h. Yang, S. Yue, H. b. Zheng, X. p. Liu, P. z. Gao, H. Qin, H. n. Xiao, ACS Appl. Mater. Interfaces, 2023, 15, 11631
- K. Wan, J. Luo, C. Zhou, T. Zhang, J. Arbiol, X. Lu, B. W. Mao, X. Zhang, J. Fransaer, *Adv. Funct. Mater.*, 2019, 29, 1900315
- H. -b. Zheng, Y. -l. Wang, P. Zhang, F. Ma, P. -z. Gao, W. -m. Guo, H. Qin, X. -p. Liu, H. -n. Xiao, Chem. Eng. J., 2021, 426, 130785
- D. Delgado, F. Bizzotto, A. Zana, M. Arenz, ChemPhysChem, 2019, 20, 3147
- 63. X. Lu, C. Zhao, Nat. Commun., 2015, 6, 6616
- Z. Yan, H. Sun, X. Chen, H. Liu, Y. Zhao, H. Li, W. Xie, F. Cheng, J. Chen, Nat. Commun., 2018, 9, 2373
- Y. Zhang, H. Liu, S. Zhao, C. Xie, Z. Huang, S. Wang, Adv. Mater., 2023, 35, 2209680
- D. Yan, C. Xia, W. Zhang, Q. Hu, C. He, B. Y. Xia, S. Wang, Adv. Energy Mater., 2022, 12, 2202317
- L. Peng, N. Yang, Y. Yang, Q. Wang, X. Xie, D. Sun-Waterhouse, L. Shang, T. Zhang, G. I. N. Waterhouse, *Angew. Chem. Int. Ed.*, 2021, 60. 24612
- M. S. Burke, M. G. Kast, L. Trotochaud, A. M. Smith, S. W. Boettcher, J. Am. Chem. Soc., 2015, 137, 3638
- D. K. Bediako, C. Costentin, E. C. Jones, D. G. Nocera, J. M. Savéant, J. Am. Chem. Soc., 2013, 135, 10492



©2025 The Authors. *Energy Lab* is published by Lab Academic Press. This is an open access article under the terms of the Creative Commons Attribution License, which permits use, distribution and reproduction in any medium, provided the original work is properly cited.